SCIENTIFIC REPORTS

Plasmon-Enhanced Light Harvesting of Chlorophylls on Near-Percolating Silver Films via One-Photon Anti-Stokes Upconversion

Ya-Lan Wang[1], Fan Nan[1], Xiao-Li Liu[1], Li Zhou[1], Xiao-Niu Peng[1], Zhang-Kai Zhou[1], Ying Yu[1], Zhong-Hua Hao[1], Yan Wu[2], Wei Zhang[3], Qu-Quan Wang[1] & Zhenyu Zhang[4,5]

[1]Department of Physics, Wuhan University, Wuhan 430072, P. R. China, [2]College of Life Sciences, Wuhan University, Wuhan 430072, P. R. China, [3]Institute of Applied Physics and Computational Mathematics, Beijing 100088, P. R. China, [4]ICQD, Hefei National Laboratory for Physical Sciences at the Microscale, University of Science and Technology of China, Hefei 230026, P. R. China, [5]Deaprtment of Physics, University of Texas, Austin, TX 78712, USA.

There exists a wealth of means of efficient utilization of solar energy in nature, with photosynthesis of chlorophylls as a prime example. Separately, artificially structured plasmonic materials are versatile in light harvesting and energy conversion. Using a simple and scalable design of near-percolating silver nanostructures, we demonstrate that the light-harvesting efficiency of chlorophylls can be drastically enhanced by tuning the plasmon frequency of the constituent silver nanoparticles to coincide with the maximal photon flux of sunlight. In particular, we show that the photon upconversion efficiency can be readily enhanced by over 20 folds, with the room-temperature fluorescence quantum yield increased by a factor of 2.63. The underlying mechanism for the upconversion enhancement is attributed to a one-electron-per-photon anti-Stokes process, involving absorption of a characteristic phonon mode of the chlorophylls. These findings suggest that chlorophylls can serve as molecular building blocks for high-efficiency light harvesting and solar energy conversion.

Light absorption is the very first step in the conversion and utilization of solar energy. Many natural and artificial materials absorb sunlight in their characteristic spectral regions to generate various types of solar energy. Photosynthetic chlorophyll, for example, is one of the most intelligent light-harvesters in nature[1–3]; it has two characteristic absorption bands at the blue and red regions, matching the maximal energy flux and near maximal photon flux of sunlight, respectively[3–5]. Considerable efforts have been devoted to investigating the underlying mechanisms of light-harvesting of the chlorophyll molecules[1,5–10] and to exploring ways to broaden their absorption regions[4–6,11–13] with the objective of further improving their overall light-harvesting efficiency for photovoltaic and photosynthetic applications.

On a separate front, plasmons, which describe collective motion of conduction electrons in metals, have gained increasing attention in the manipulation and control of interaction of light with matter, particularly with nanoscale metal systems[14–32]. As one of the versatile systems, a metallic nanomaterial may generate both localized and delocalized modes of plasmons, which can enhance Raman scattering and fluorescence, and, as a result, help to improve the efficiency of solar energy devices[33–45]. Localized surface plasmon resonance (LSPR) that exists at a surface of a metal nanostructure can intensify light scattering and enhance light concentration around the structure. Delocalized surface plasmons, on the other hand, can help to trap light at the interfaces. All these effects are favorable for enhancing optical absorption of the light harvesters[6,46–49].

In the present work, we integrate the merits of photosynthetic chlorophyll and plasmonics through construction of systems that consist of chlorophyll molecules coated onto readily accessible and scalable nanostructured silver films. We demonstrate that the light-harvesting efficiency of chlorophyll can be greatly increased via a plasmon-enhanced anti-Stokes process involving simultaneous absorption of a low-energy photon and a characteristic phonon mode of the chlorophyll molecules[50,51]. The nanosystem used in our study is illustrated in **Fig. 1a**. We adjust the nanostructured silver films to be close to the percolation regime in order to generate a significantly broadened LSPR around the red absorption band of chlorophyll, which is of far-reaching potential
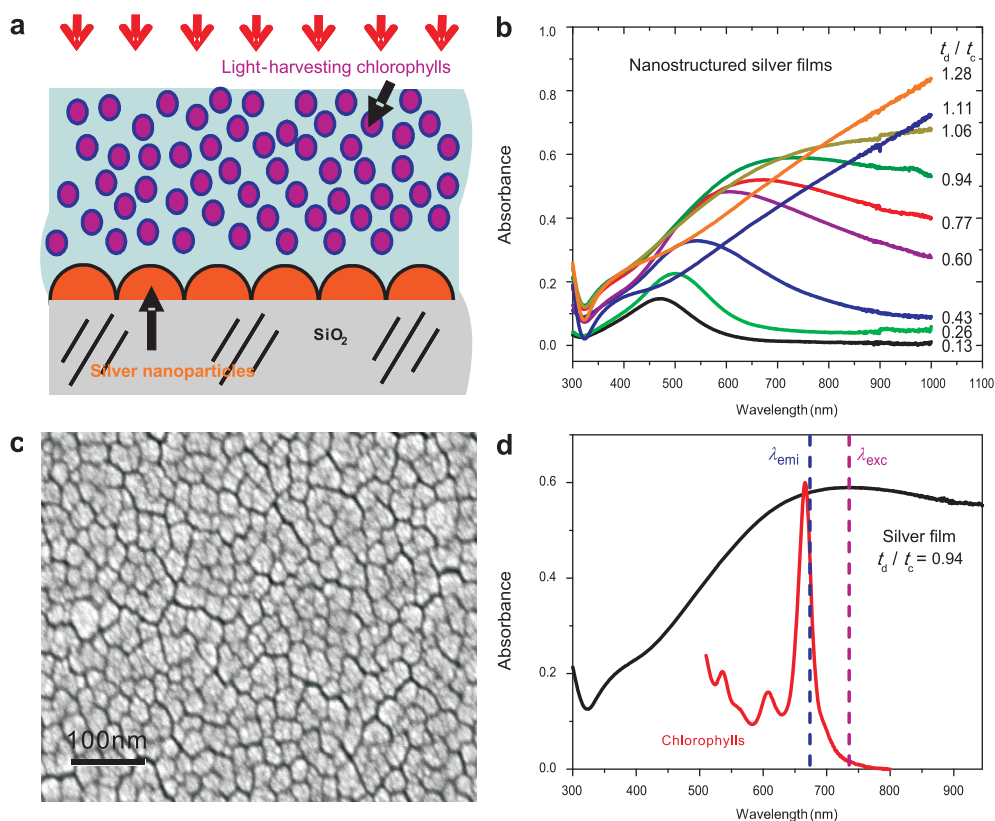
Figure 1 | **Nanostructures and absorption spectra of the samples.** (a) Illustration of the nanostructure of the sample. (b) Absorption spectra of the nanostructured silver films with normalized deposition time t_d/t_c ranging from 0.13 to 1.28. The central peak of the LSPR (λ_{SP}) of the silver films shifts from 470 nm to 735 nm as t_d/t_c increases from 0.13 to 0.94. (c) SEM image of the near-percolating silver film with normalized deposition time $t_d/t_c =$ 0.94. The average size of the silver nanoparticles is about 40 nm, and the average gap distance between the silver nanoparticles is about 4 nm. (d) Absorption spectra of the silver film ($t_d/t_c =$ 0.94) and chlorophylls. The dashed lines indicate the laser excitation wavelength 735 nm and Chl-a emission wavelength ~675 nm.

significance because this band coincides with the region of the maximal photon flux of sunlight. We also introduce a theoretical mode, based on the measured fluorescence intensity and decay rate, to calculate and analyze the quantum yield of the plasmon-enhanced fluorescence and excitation energy transfer in the nanosystem. We find that the upconversion efficiency can be readily enhanced by over 20 folds, and the fluorescence quantum yield increased by a factor of 2.63 at room temperature. These findings demonstrate that the chlorophyll molecules assisted by plasmons can be even better light harvesters around the red/infrared region than those unassisted by plasmons. Our study serves as another example of how solar energy can be utilized more efficiently when a man-made nanomaterial system works together with a natural material system.

Results

Structural design and tunable plasmon resonance. Two types of chlorophyll samples were used in our study: natural chlorophyll mixtures (Chl-mix) and pure Chl-a. The red absorption bands of Chl-mix and Chl-a are near 665 nm and 662 nm, respectively. The chlorophyll samples and polyvinylpyrrolidone (PVP) were dissolved in ethanol and the prepared solution was spin-coated onto the nanostructured silver films grown on SiO_2 substrates. The thickness of the Chl:PVP films was approximately 50 nm. The silver films were deposited on the fused quartz (SiO_2) substrates by sputtering. The plasmon resonance wavelength, λ_{SP}, of the silver films was adjusted by controlling the sputtering deposition time t_d. **Figure 1b** shows the absorption spectra of the silver films with normalized deposition time t_d/t_c (where $t_c \approx$ 118 s is the

deposition time for the percolation threshold) ranging from 0.13 to 1.28. Only discontinuous (disconductive) silver films ($t_d/t_c <$ 1) show a LSPR peak. As t_d/t_c increases from 0.13 to 0.94, the LSPR band of the silver films is broadened and the central peak of LSPR shifts from ~470 to ~730 nm. The absorbance of the conductive silver films ($t_d/t_c >$ 1) increases monotonously as the wavelength increases from the visible to near infrared region (450 ~ 1000 nm). The Chl:PVP coating layer on the silver film leads to a red shift in the LSPR. Quantitatively, the near-percolating film has smaller red-shift induced by the coating dielectric layer due to smaller gap distances between the silver nanoparticles. **Figure 1c** is a scanning electron microscopy (SEM) image of the near-percolating films with normalized deposition time $t_d/t_c =$ 0.94. It shows fractal-nanostructured silver clusters with inhomogeneous size and shape distributions of the constituent nanoparticles, and the average size of the silver nanoparticles is ~40 nm, with an average gap separation of ~4 nm[52]. This near-percolating film is discontinuous (non-conductive) with a filling factor of ~0.68 and a fractal dimension of ~1.6[53,54], which supports both localized and delocalized plasmon modes[55]. The LSPR of the silver film is significantly broadened by the near-percolating fractal nanostructure, as shown in **Fig. 1d**, and it spans from the visible region to the near infrared region with a central peak, λ_{SP}, at ~730 nm, which is around both the region of maximal photon flux of sunlight and the red-absorption band of chlorophylls. The nanostructured films strongly enhance the local fields in a large spectral range, including the chlorophyll emission wavelength ($\lambda_{emi} =$ 675 nm) and the laser excitation wavelength ($\lambda_{exc} =$ 735 nm).
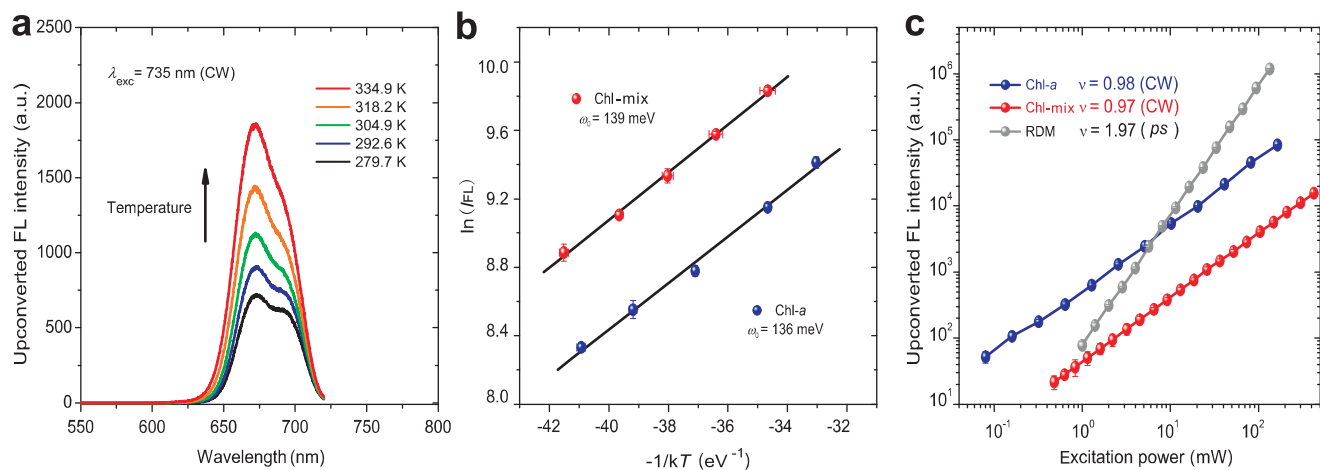
Figure 2 | One-photon upconversion of the chlorophylls in the absence of a silver film excited by a continuous wave laser at the wavelength 735 nm.
(a) Temperature-dependent upconverted fluorescence spectra of the chlorophylls suspensions. (b) The logarithmic fluorescence intensity $\ln(I_{FL})$ as a function of $-1/kT$. The slope, $\omega_0 = \partial \ln I_{FL}/\partial(-1/kT)$, corresponds to the averaged phonon energy captured in the anti-Stokes upconversion process of the chlorophylls. (c) The excitation power dependence of the upconversion fluorescence intensities of the Chl-mix, pure Chl-a and RDM-b. The power index, $v = \partial \ln I_{FL}/\partial \ln p_{exc}$, indicates the number of photons involved in the anti-Stokes upconversion processes.

One-photon anti-Stokes upconversion of the chlorophyll molecules. Figure 2a shows the upconversion fluorescence spectra of the Chl-mix suspensions in ethanol, which is excited by a continuous wave (CW) laser with an excitation wavelength $\lambda_{exc} = 735$ nm. As shown in **Fig. 2a**, the peak intensity (I_{FL}) of the upconversion fluorescence at ~673 nm is increased by ~160% as the sample temperature is increased from 279.7 K to 334.9 K. This intensity increase is attributed to the phonon-assisted processes during anti-Stokes upconversion[56,57]. We found that $\ln I_{FL}$ is linearly dependent on $-1/kT$, as shown in **Fig. 2b**, where k is the Boltzmann constant. The proportionality constant, $\omega_0 = \partial \ln I_{FL}/\partial(-1/kT)$, which is a measure of the average phonon energy involved in the anti-Stokes upconversion of the Chl-mix and Chl-a is found to be 139 and 136 meV, respectively. These values are in good agreement with the measured Raman shift of the corresponding phonon mode; the latter is ~133 meV[4].

Figure 2c shows the excitation-power dependence of the fluorescence peak intensity (I_{FL}) of the Chl-mix and Chl-a with CW excitation, and the reference sample rhodamine b (RDM-b) with ps-pulse excitation. The emission power index $v = \partial \ln I_{FL}/\partial \ln p_{exc}$ of the Chl-mix and Chl-a is measured to be ~0.97 and 0.98, respectively,

even when the time-averaged excitation power density p_{exc} is decreased to as low as 0.5 mW/cm². This linear scaling is distinctly different from those for upconversion via two-photon absorption, such as for the reference sample RDM-b, where $v \sim 2$ in the weak excitation region[11,12]. This linear scaling indicates that the upconversion fluorescence of chlorophylls is induced by one-photon absorption. The dependencies of chlorophyll upconversion on the temperature and excitation power indicate that one electron in chlorophylls can be pumped to a high energy level by simultaneously absorbing a single low-energy photon in the near infrared region and a phonon of the sample.

Plasmon-enhanced light harvesting of the chlorophyll molecules. Next, we used the nanostructured silver films to enhance the light-harvesting efficiency of the Chl-mix:PVP. **Figure 3a** shows the upconversion fluorescence spectra of Chl-mix:PVP coated on the silver films with normalized deposition time of $t_d/t_c = 0$, 0.26, 0.43, 0.60, 0.77, 0.94, 1.06, 1.11, and 1.28. The upconversion fluorescence of the Chl-mix:PVP film was strongly enhanced by the use of discontinuous Ag island films ($0.26 < t_d/t_c < 0.94$, 600 nm $< \lambda_{SP} < 740$ nm), as shown in **Fig. 3a**, but weakly
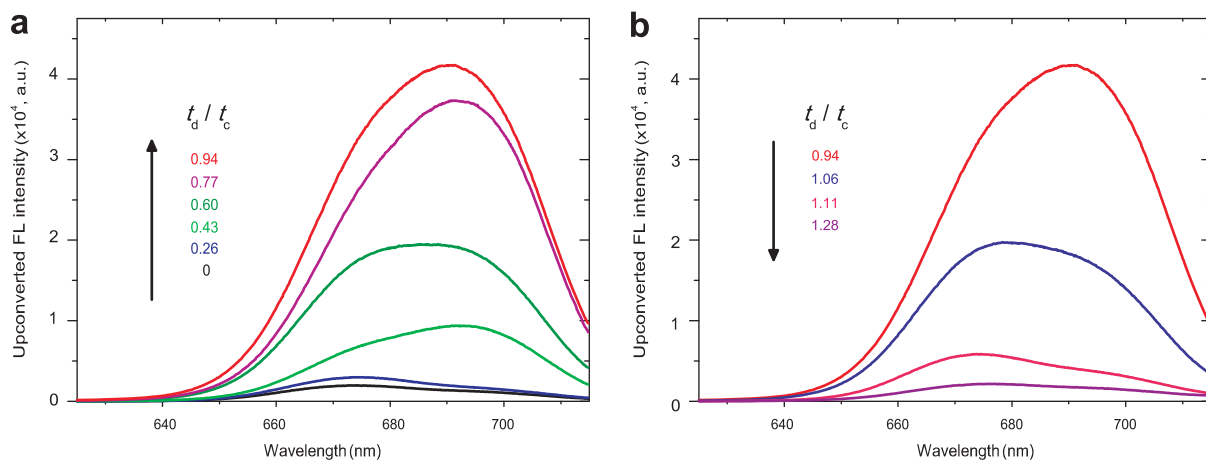

Figure 3 | Plasmon-enhanced one-photon anti-Stokes upconversion of Chl-mix:PVP films excited by a CW laser with $\lambda_{exc} = 735$ nm. Upconverted fluorescence spectra of the Chl-mix:PVP on the silver films with $t_d/t_c = 0$, 0.26, 0.43, 0.60, 0.77, and 0.94 (a), and $t_d/t_c = 0.94$, 1.06, 1.11, and 1.28 (b). Enhancement of upconverted fluorescence reaches the maximum for the near-percolating silver film ($t_d/t_c = 0.94$).

enhanced by the use of continuous Ag films ($t_d/t_c > 1.06$) , as shown in **Fig. 3b**. The strongest fluorescence occurs at $t_d/t_c = 0.94$ and the corresponding emission peak is slightly shifted from 675 nm to 690 nm, where the enhancement factor $R_{FL} = I_{FL} / I_{FL}^{(0)}$ reaches the maximum value of 21.5. This enhanced fluorescence of chlorophyll molecules in the vicinity of silver film is mainly attributed to the efficient excitation of excitons to the higher levels via plasmon-induced enhancements of local excitation field and exciton-phonon coupling in the anti-Stokes processes.

Plasmon-enhanced fluorescence decay rate. The fluorescence decay rate of chlorophylls is also enhanced by the silver films. The total decay rate, Γ, is the sum of the radiative rate, γ_{rad}, and the nonradiative rate, k_{nr}. We use $\Gamma^{(int)}$, $\Gamma^{(0)}$, and Γ to denote the total decay rates of chlorophylls suspended in ethanol, and that of Chl-mix:PVP in the absence and presence of the silver films, respectively. From the recorded fluorescence decay traces of the three samples shown in **Fig. 4**, we obtained the values of the three decay rates: $\Gamma^{(int)} = 0.160$ ns^{-1}, $\Gamma^{(0)} = 0.323$ ns^{-1}, and $\Gamma = 0.980$ ns^{-1} ($t_d/t_c = 0.94$). $\Gamma^{(0)}$ is about twice as large as $\Gamma^{(int)}$ due to increased nonradiative energy relaxation between the chlorophyll molecules in the solid PVP films. Γ is much larger than $\Gamma^{(0)}$, and the decay rate enhancement factor $R_\Gamma = \Gamma/\Gamma^{(0)}$ reaches 3.04 due to interaction between the chlorophylls and silver films.

The radiative rate is increased by the plasmon-exciton interaction with the relationship $\gamma_{rad}/\gamma_{rad}^{(0)} = |f(\lambda_{emi})|^2$, where $f(\lambda_{emi})$ is the local field enhancement factor at the emission wavelength. The increase of nonradiative rate is described by $k_{nr} = k_{nr}^{(0)} + \Delta k_{nr}$, where Δk_{nr} is the nonradiation energy transfer rate from the chlorophylls to the metal film. We found that the total decay rate enhancement factor R_Γ reaches the maximum 3.44 when λ_{SP} of the silver film grown at $t_d/t_c = 0.77$ near the chlorophyll emission wavelength. As t_d/t_c increases from 0.77 to 1.28 (**Fig. 5**), even though the morphology of the films varies from being discontinuous to semi-continuous, the decay rate enhancement factor R_Γ decreases monotonically from 3.44 to about 1. This observation indicates that the enhanced decay rate can be mainly attributed to the radiative rate increased by the local field enhancement of the silver films. This increased radiative emission is the origin of the observed red-shifting (from 675 nm to 690 nm) of the fluorescence peak of the chlorophyll molecules on the silver films.
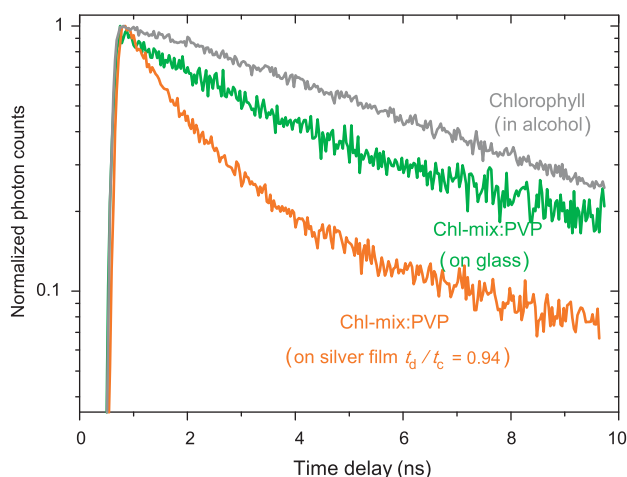

Figure 4 | Time-resolved fluorescence decay traces of chlorophylls and Chl-mix:PVP films excited by using a picosecond pulse laser and recorded at the emission wavelength $\lambda_{emi} = 675$ nm. Normalized fluorescence decay traces of the Chl-mix suspended in ethanol (decay rate $\Gamma^{(int)} = 0.160$ ns^{-1}), the Chl-mix:PVP film on blank fused quartz substrate ($\Gamma^{(0)} = 0.323$ ns^{-1}), and the Chl-mix:PVP on a near-percolating silver film with $t_d/t_c = 0.94$ ($\Gamma = 0.980$ ns^{-1}).
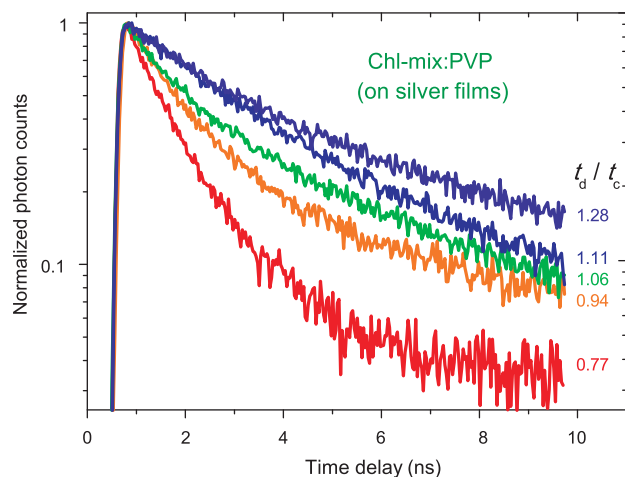

Figure 5 | Time-resolved fluorescence decay traces of Chl-mix:PVP films excited by using a picosecond pulse laser and recorded at the emission wavelength $\lambda_{emi} = 675$ nm. Normalized fluorescence decay traces of Chl-mix:PVP on the silver films with $t_d/t_c = 0.77$, 0.94, 1.11, and 1.28, respectively. The decay rate Γ reaches the maximum when λ_{SP} of silver film is around $\lambda_{emi} = 675$ nm ($t_d/t_c = 0.77$).

Discussion

The fluorescence quantum yield defined as $Q_{FL} = \gamma_{rad}/(\gamma_{rad} + k_{nr})$ represents the fraction of the excitons relaxed by radiative decay relative to the total decay, and quantitatively describes the emission efficiency. The plasmon resonances enhance the fluorescence intensity, the decay rate, as well as the quantum yield. The quantum yield enhancement, R_{QY}, the fluorescence enhancement factor, R_{FL}, and the decay rate enhancement factor, R_Γ, are related through the following equations[23,58],

$$R_{FL} = R_{QY}|f(\lambda_{exc})|^2, \qquad (1)$$

$$R_{QY} = (R_\Gamma)^{-1}|f(\lambda_{emi})|^2, \qquad (2)$$

where $|f(\lambda_{exc})|$ is the local field enhancement factor at the excitation wavelength. Combining equations (1) and (2), the quantum yield enhancement is obtained as,

$$R_{QY} = \left|\frac{f(\lambda_{emi})}{f(\lambda_{exc})}\right|\left(\frac{R_{FL}}{R_\Gamma}\right)^{1/2}. \qquad (3)$$

If the separation of the excitation and emission wavelength is small and the plasmon resonance of the metal nanostructure is broadened, then the differences of both absorption coefficients α and field enhancements at the two wavelengths are very small[52,59]. This leads to a good approximation, $|f(\lambda_{emi})/f(\lambda_{exc})|^2 \approx \alpha(\lambda_{emi})/\alpha(\lambda_{exc})$. In this case, R_{QY} can be directly calculated from the measured R_{FL} and R_Γ with a very simple relationship,

$$R_{QY} \approx \left(\frac{\alpha(\lambda_{emi})}{\alpha(\lambda_{exc})}\right)^{1/2}\left(\frac{R_{FL}}{R_\Gamma}\right)^{1/2}. \qquad (4)$$

For the anti-Stokes upconversion of the chlorophyll molecules, the difference in the wavelengths, $\Delta\lambda = \lambda_{emi} - \lambda_{exc}$, is only 60 nm resulting in a very small difference in the absorptions $\alpha(\lambda_{emi})$ and $\alpha(\lambda_{exc})$. Meanwhile, for the near-percolating nanostructured silver films used in our studies, the inhomogeneous size and shape distributions of the constituent silver nanoparticles led to significantly-broadened plasmon resonances as shown in **Fig. 1b**. The quantum yield enhancement R_{QY} of Chl-mix:PVP is calculated accordingly to be 2.63 based on the experimentally measured results of $R_{FL} = 21.5$ and $R_\Gamma = 3.04$ for the silver films with $t_d/t_c = 0.94$.
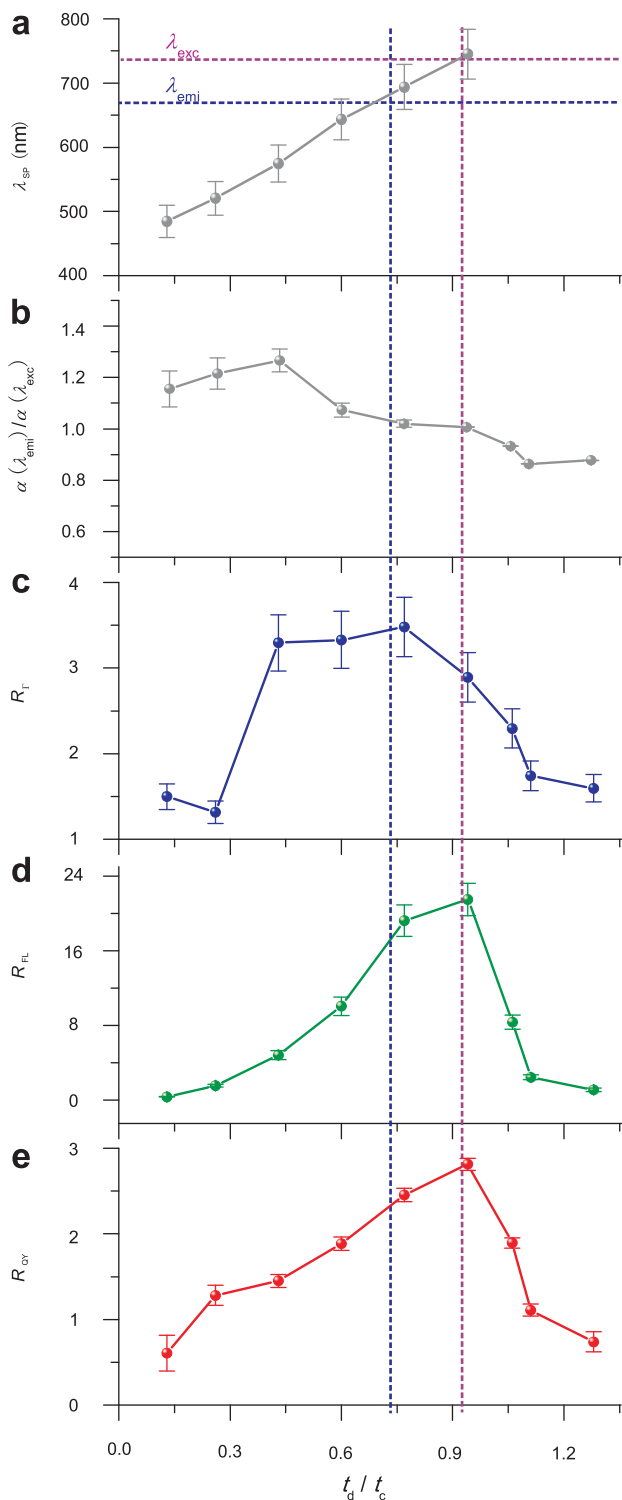
Figure 6 synoptically presents plasmon resonance absorption and three enhancement factors (R_{FL}, R_Γ, and R_{QY}) of fluorescence, decay rate and quantum yield of Chl-mix:PVP/Ag as a function of normalized deposition time t_d/t_c of the silver films. The absorption ratio $\alpha(\lambda_{emi})/\alpha(\lambda_{exc})$ is very close to 1 when the plasmon resonance wavelength λ_{SP} is around λ_{emi} and λ_{exc} (**Fig. 6a** and **6b**). R_Γ reaches the maximum value of 3.44 when $t_d/t_c = 0.77$ (**Fig. 6c**), and R_{FL} and R_{QY} reaches the maxima 21.5 and 2.63 when λ_{SP} is tuned to around $\lambda_{exc} = 735$ nm for the near-percolating silver film ($t_d/t_c = 0.94$) (**Figs. 6d** and **6e**). When $t_d/t_c > 1$, the silver films become semi-continuous (conductive), the plasmonic resonance absorption vanishes, and both R_{FL} and R_{QY} dramatically decrease. Based on these observations, we conclude that the dominant mechanism of the maximal anti-Stokes fluorescence is plasmon-enhanced excitation, and this excitation enhancement is commonly reported in the Stokes processes. We also notice that the silver film with $t_d/t_c = 0.94$ is close to the percolating regime, so the percolating effect could be partially involved in fluorescence enhancement, which remains to be further studied.

For comparison, the upconversion parameters of pure Chl-a have also been measured, as listed in **Table 1** along with the corresponding values of Chl-mix. These results confirm that the fluorescence of the Chl-mix can be attributed to Chl-a. The enhancement factors of the fluorescence intensity and the decay rate of the Chl-a:PVP samples are measured to be $R_{FL} = 14.6$ and $R_\Gamma = 3.71$, respectively. Compared with the Chl-mix, the Chl-a samples have a larger R_Γ, owing to a smaller $\Gamma^{(0)}$, and smaller R_{QY} and R_{FL} due to the higher $Q_{FL}^{(0)}$. Our results suggest that natural Chl-mix should be preferred over pure Chl-a as the material of choice for practical solar energy conversion, due to their much lower cost and higher plasmon enhancement factor.

So far we have shown that (i) the near-percolating silver films have broadened LSPR around the red-absorption band of chlorophylls, where the maximal photon flux of sunlight is located; (ii) both the light-harvesting efficiency of chlorophylls and the fluorescence quantum yield are significantly improved by the near-percolating silver films, and the underlying mechanism for the plasmon-enhanced upconversion is identified to be via a one-photon anti-Stokes process, involving the absorption of a characteristic phonon mode of the chlorophylls, which effectively generates one higher-level electron per lower-energy photon; and (iii) the theoretical model proposed here for the calculation of quantum yield enhancement offers a useful tool to study energy transfer and fluorescence enhanced by metallic nanostructures with broadened LSPR.

Finally, we would like to point out that the photon-excited carriers assisted by plasmon resonances could in principle be efficiently transferred to other proper contacts/leads with much faster transfer rates than the radiative rate when the chlorophylls are used in potential photoelectronic and photocatalytic devices. Therefore, plasmon-enhanced efficient generation of photoelectrons via one-photon anti-Stokes processes as demonstrated here may offer new opportunities in developing novel photovoltaic and photocatalytic devices. Taken together, the present study suggests that chlorophylls, assisted by near-percolating metal films through their enhancement of the local fields in a broadened spectral region, can serve as a molecular building block in artificial photosynthetic systems for high-efficiency sunlight harvesting and solar energy conversion.

Figure 6 | **Plasmon resonance absorption and three enhancement factors (R_{FL}, R_Γ, and R_{QY}) of fluorescence, decay rate and quantum yield of Chl-mix:PVP on discontinuous (non-conductive) and semi-continuous (conductive) silver films prepared with different deposition time.** Normalized deposition time dependences of the plasmon resonance wavelength of Chl-mix:PVP/Ag (a), absorption ratio $R_\alpha = \alpha(\lambda_{emi})/\alpha(\lambda_{exc})$ (b), decay rate enhancement R_Γ (c), fluorescence enhancement R_{FL} (d), and quantum yield enhancement R_{QY} (e). Two dashed lines indicate that $\lambda_{emi} = 675$ nm and $\lambda_{exc} = 735$ nm. Plasmonic resonance absorption vanishes when $t_d/t_c > 1$.

Table 1 | Anti-Stokes fluorescence parameters of Chl-mix and Chl-a

Sample	v	ω_0 [meV]	$\Gamma^{(0)}$ [ns^{-1}]	Γ [ns^{-1}]	R_Γ	R_{FL}	R_{QY}
Chl-mix	0.97	139	0.323	0.980	3.04	21.5	2.63
Chl-a	0.98	136	0.200	0.742	3.71	14.6	1.94

Methods

Preparation of nanostructured silver films and Chl:PVP coating films. The silver films were deposited by sputtering in an argon atmosphere with a sputtering pressure of 5 Pa and a power of 1.5 kV × 7 mA. The average deposition rate was about 4.0 nm/min. The nanoparticle size and LSPR of the films were adjusted by controlling the sputtering deposition time t_d, whose range was from 15 s to 150 s. The nanostructured films were analyzed using SEM on a FEG SEM Sirion 200 operated at an accelerating voltage of 25.0 kV. The Chl-mix used in our studies were purchased from Shandong Guangtongbao Pharmaceuticals Co., Ltd (China). The purified Chl-a (purity ≥ 85%), which was made from spinach, was purchased from Sigma-Aldrich (USA). The content of the Chl-mix was determined by measuring the absorption spectra of the samples. The calculated Chl-a, Chl-b and carotenoid content was approximately 2.73%, 0.61% and 0.82%, respectively. As expected, Chl-a contributed the most to the upconversion fluorescence. The chlorophylls (0.5 mg/ml) and PVP (33 mg/ml) were separately dissolved in ethanol. The prepared chlorophylls and PVP solutions were mixed with a volume ratio of 1.0 : 1.0, and the mixture was spin-coated onto the nanostructured silver films on a fused quartz substrate. The thickness of the Chl:PVP film, measured using a profilometer (Talysurf Profiler-S4C, Taylor Hobson), was approximately 50 nm when the spin-rotation rate was 1500 r/min.

Optical measurements. The absorption spectra of the silver films and the Chl:PVP coating films were recorded at room temperature on a Varian Cary 5000 spectrometer. To measure fluorescence, a wavelength-tunable Ti:sapphire laser (Mira 900, Coherent) was used as the excitation source; the laser can run in CW mode and mode-locked pulse mode. The pulse width was ~2.5 ps, and the repetition rate was 76 MHz. The incident angle of the excitation source was ~80°. The upconversion fluorescence of the chlorophylls was excited by the CW laser with wavelengths from 725 nm to 775 nm. The down-conversion fluorescence of the chlorophylls was excited by a 415 nm laser, generated by focusing a 830 nm mode-locked pulse laser into a second harmonic generation (SHG) system (HarmoniXX, APE GmbH). The chlorophyll fluorescence was measured in reflection mode and recorded via spectrometry (Spectrapro 2500i, Acton) with a liquid-nitrogen-cooled CCD (SPEC-10, Princeton). A long-wave pass filter or a short-wave pass filter was used to filter the excitation laser. The time-resolved fluorescence decay traces were recorded using a time-correlated single-photon counting system (PicoQuant GmbH).

1. Fong, F. K. Molecular basis for the photosynthetic primary process. *Proc. Natl. Acad. Sci.* **71**, 3692–3695 (1974).
2. Fong, F. K. Molecular symmetry and exciton interaction in photosynthetic primary events. *Appl. Phys.* **6**, 151–166 (1975).
3. Gates, D. M., Keegan, H. J., Schleter, J. C. & Weidner, V. R. Spectral properties of plants. *Appl. Opt.* **4**, 11–20 (1965).
4. Thomas, L. L., Kim, J. H. & Cotton, T. M. Comparative study of resonance Raman and surface-enhanced resonance Raman chlorophyll a spectra using Soret and red excitation. *J. Am. Chem. Soc.* **112**, 9378–9386 (1990).
5. Leupold, D. et al. Two-photon excited fluorescence from higher electronic states of chlorophylls in photosynthetic antenna complexes: A new approach to detect strong excitonic chlorophyll *a/b* coupling. *Biophys. J.* **82**, 1580–1585 (2002).
6. Mackowski, S. et al. Metal-enhanced fluorescence of chlorophylls in single light-harvesting complexes. *Nano Lett.* **8**, 558–564 (2008).
7. Pascal, A. A. et al. Molecular basis of photoprotection and control of photosynthetic light-harvesting. *Nature* **436**, 134–137 (2005).
8. Liu, Z. F. et al. Crystal structure of spinach major light-harvesting complex at 2.72 angstrom resolution. *Nature* **428**, 287–292 (2004).
9. Moser, S. et al. Fluorescent chlorophyll catabolites in bananas light up blue halos of cell death. *Proc. Natl. Acad. Sci.* **106**, 15538–15543 (2009).
10. Zeng, L., Xing, D., Zhang, L., Li, Q. & Wang, C. Spectroscopic studies on the origination of the peak at 730 nm in delayed fluorescence of chloroplasts. *Luminescence* **22**, 387–392 (2007).
11. Zimmermann, J., Linden, P. A., Vaswani, H. M., Hiller, R. G. & Fleming, G. R. Two-photon excitation study of peridinin in benzene and in the peridinin chlorophyll a-protein (PCP). *J. Phys. Chem. B* **106**, 9418–9423 (2002).
12. Shima, S. et al. Two-photon and fluorescence spectroscopy and the effect of environment on the photochemical properties of peridinin in solution and in the peridinin-chlorophyll-protein from Amphidinium carterae. *J. Phys. Chem. A* **107**, 8052–8066 (2003).
13. Prodan, E., Radloff, C., Halas, N. J. & Nordlander, P. A hybridization model for the plasmon response of complex nanostructures. *Science* **302**, 419–422 (2003).
14. Tanaka, Y., Sanada, A. & Sasaki, K. Nanoscale interference patterns of gap-mode multipolar plasmonic fields. *Scientific Reports* **2** (764), 10.1038 (2012).
15. Sun, M., Zhang, Z., Zheng, H. & Xu, H. In-situ plasmon-driven chemical reactions revealed by high vacuum tip-enhanced Raman spectroscopy. *Scientific Reports* **2** (647), 10.1038 (2012).
16. Fan, J. A. et al. Self-assembled plasmonic nanoparticle clusters. *Science* **328**, 1135–1138 (2010).
17. Dulkeith, E. et al. Fluorescence quenching of dye molecules near gold nanoparticles: radiative and nonradiative effects. *Phys. Rev. Lett.* **89**, 203002 (2002).
18. Louis, C. et al. Gold nano-antennas for increasing luminescence. *Adv. Mater.* **16**, 2163–2166 (2004).
19. Liu, H. et al. Single molecule detection from a large-scale SERS-active $Au_{79}Ag_{21}$ substrate. *Scientific Reports* **1** (112), 10.1038 (2011).
20. Heaton, R. J., Peterson, A. W. & Georgiadis, R. M. Electrostatic surface plasmon resonance: Direct electric field-induced hybridization and denaturation in monolayer nucleic acid films and label-free discrimination of base mismatches. *Proc. Natl. Acad. Sci.* **98**, 3701–3704 (2001).
21. Peng, S., McMahon, J. M., Schatz, G. C., Gray, S. K. & Sun, Y. G. Reversing the size-dependence of surface plasmon resonances. *Proc. Natl. Acad. Sci.* **107**, 14530–14534 (2010).
22. Kühn, S., Håkanson, U., Rogobete, L. & Sandoghdar, V. Enhancement of single-molecule fluorescence using a gold nanoparticle as an optical nanoantenna. *Phys. Rev. Lett.* **97**, 017402 (2006).
23. Bardhan, R., Grady, N. K., Cole, J. R., Joshi, A. & Halas, N. J. Fluorescence enhancement by Au nanostructures: Nanoshells and nanorods. *ACS Nano* **3**, 744–752 (2009).
24. Jun, Y. C., Huang, K. C. Y. & Brongersma, M. L. Plasmonic beaming and active control over fluorescent emission. *Nat. Commun.* **2**, 283 (2011).
25. Zhang, W., Li, Z., Gu, B., Zhang, Z. & Xu, H. Ag@SiO₂ core-shell nanoparticles for probing spatial distribution of electromagnetic field enhancement via surface-enhanced Raman scattering. *ACS Nano* **3**, 3493–3496 (2009).
26. Wang, H. F. et al. In vitro and in vivo two-photon luminescence imaging of single gold nanorods. *Proc. Natl. Acad. Sci.* **102**, 15752–15756 (2005).
27. Oulton, R. F. et al. Plasmon lasers at deep subwavelength scale. *Nature* **461**, 629–632 (2009).
28. Van Duyne, R. P. Molecular plasmonics. *Science* **306**, 985–986 (2004).
29. Cade, N. I., Ritman-Meer, T. & Richards, D. Strong coupling of localized plasmons and molecular excitons in nanostructured silver films. *Phys. Rev. B* **79**, 241404(R) (2009).
30. Kinkhabwala, A. et al. Large single-molecule fluorescence enhancements produced by a bowtie nanoantenna. *Nat. Photonics.* **3**, 654–657 (2009).
31. Zhang, J., Li, D., Chen, R. & Xiong, Q. Laser cooling of a semiconductor by 40 kelvin. *Nature* **493**, 504–508 (2013).
32. Zhang, Q. et al. Highly enhanced exciton recombination rate by strong electron–phonon coupling in single ZnTe nanobelt. *Nano Lett.* **12**, 6420–6427 (2012).
33. Atwater, H. A. & Polman, A. Plasmonics for improved photovoltaic devices. *Nat. Mater.* **9**, 205–213 (2010).
34. Schuller, J. A. et al. Plasmonics for extreme light concentration and manipulation. *Nat. Mater.* **9**, 193–204 (2010).
35. Knight, M. W., Sobhani, H., Nordlander, P. & Halas, N. J. Photodetection with active optical antennas. *Science* **332**, 702–704 (2011).
36. Ferry, V. E., Munday, J. N. & Atwater, H. A. Design considerations for plasmonic photovoltaics. *Adv. Mater.* **22**, 4794–4808 (2010).
37. Stuart, H. R. & Hall, D. G. Absorption enhancement in silicon-on-insulator waveguides using metal island films. *Appl. Phys. Lett.* **69**, 2327–2329 (1996).
38. Derkacs, D. et al. Nanoparticle-induced light scattering for improved performance of quantum-well solar cells. *Appl. Phys. Lett.* **93**, 091107 (2008).
39. Munday, J. N. & Atwater, H. A. Large integrated absorption enhancement in plasmonic solar cells by combining metallic gratings and antireflection coatings. *Nano Lett.* **11**, 2195–2201 (2011).
40. Ding, B., Lee, B. J., Yang, M., Jung, H. S. & Lee, J.-K. Surface-plasmon assisted energy conversion in dye-sensitized solar cells. *Adv. Energy Mater.* **1**, 415–421 (2011).
41. Heidel, T. D. et al. Surface plasmon polariton mediated energy transfer in organic photovoltaic devices. *Appl. Phys. Lett.* **91**, 093506 (2007).
42. Echtermeyer, T. J. et al. Strong plasmonic enhancement of photovoltage in grapheme. *Nat. Commun.* **2**, 458 (2011).
43. Ferry, V. E., Sweatlock, L. A., Pacifici, D. & Atwater, H. A. Plasmonic nanostructure design for efficient light coupling into solar cells. *Nano Lett.* **8**, 4391–4397 (2008).
44. Luque, A. & Marti, A. Increasing the efficiency of ideal solar cells by photon induced transitions at intermediate levels. *Phys. Rev. Lett.* **78**, 5014–5017 (1997).
45. Mühlschlegel, P., Eisler, H. J., Martin, O. J. F., Hecht, B. & Pohl, D. W. Resonant optical antennas. *Science* **308**, 1607–1609 (2005).
46. Nieder, J. B., Bittl, J. B. R. & Brecht, M. Fluorescence studies into the effect of plasmonic interactions on protein function. *Angew. Chem. Int. Ed.* **49**, 10217–10220 (2010).
47. Govorov, A. O. & Carmeli, I. Hybrid structures composed of photosynthetic system and metal nanoparticles: plasmon enhancement effect. *Nano Lett.* **7**, 620–625 (2007).
48. Mackowski, S. Hybrid nanostructures for efficient light harvesting. *J. Phys.: Condens. Matter* **22**, 193102 (2010).
49. Biesso, A., Qian, W., Huang, X. & El-Sayed, M. A. Gold nanoparticles surface plasmon field effects on the proton pump process of the bacteriorhodopsin photosynthesis. *J. Am. Chem. Soc.* **131**, 2442–2443 (2009).
50. Baibarac, M., Massuyeau, F., Wery, J., Baltog, I. & Lefrant, S. Raman scattering and anti-Stokes luminescence in poly-paraphenylene vinylene/carbon nanotubes composites. *J. Appl. Phys.* **111**, 083109 (2012).
51. Drachev, V. P. et al. Low-threshold lasing and broad-band multiphoton-excited light emission from Ag aggregate-adsorbate complexes in microcavity. *J. Mod Opt.* **49**, 645–662 (2002).
52. Kulakovich, O. et al. Enhanced luminescence of CdSe quantum dots on gold colloids. *Nano Lett.* **2**, 1449–1452 (2002).

6

53. Stockman, M. I., Pandey, L. N., Muratov, L. S. & George, T. F. Giant fluctuations of local optical fields in fractal clusters. *Phys. Rev. Lett.* **72**, 2486–2489 (1994).
54. Ding, S., Wang, X., Chen, D. J. & Wang, Q. Q. Optical percolation and nonlinearity of sputtered Ag island films. *Opt. Express* **14**, 1541–1546 (2006).
55. Seal, K. *et al.* Coexistence of localized and delocalized surface plasmon modes in percolating metal films. *Phys. Rev. Lett.* **97**, 206103 (2006).
56. Le, F. *et al.* Metallic nanoparticle arrays: A common substrate for both surface-enhanced Raman scattering and surface-enhanced infrared absorption. *ACS Nano* **2**, 707–718 (2008).
57. Hasegawa, M., Shiina, T., Terazima, M. & Kumazaki, S. Selective excitation of photosystems in chloroplasts inside plant leaves observed by near-infrared laser-based fluorescence spectral microscopy. *Plant Cell Physiol.* **51**, 225–238 (2010).
58. Govorov, A. O. *et al.* Exciton−plasmon interaction and hybrid excitons in semiconductor−metal nanoparticle assemblies. *Nano Lett.* **6**, 984–994 (2006).
59. Yagil, Y. & Deutscher, G. Transmittance of thin metal films near the percolation threshold. *Thin Solid Films* **152**, 465–471 (1987).

Acknowledgements

Author contributions

Additional information

How to cite this article: Wang, Y. *et al.* Plasmon-Enhanced Light Harvesting of Chlorophylls on Near-Percolating Silver Films via One-Photon Anti-Stokes Upconversion. *Sci. Rep.* **3**, 1861; DOI:10.1038/srep01861 (2013).